Nanoparticle transport within non-Newtonian fluid flow in porous media

Takshak Shende

Department of Chemical Engineering, The University of Manchester, Manchester, United Kingdom

Deepak Mangal

Department of Chemical and Biomolecular Engineering, University of Houston, Houston, Texas 77004, USA

Jacinta C. Conrad

Department of Chemical and Biomolecular Engineering, University of Houston, Houston, Texas 77004, USA

Vahid Niasar

Department of Chemical Engineering, The University of Manchester, Manchester, United Kingdom

Masoud Babaei[*]

Department of Chemical Engineering, The University of Manchester, Manchester, United Kingdom

Control over dispersion of nanoparticles in polymer solutions through porous media is important for subsurface applications such as soil remediation and enhanced oil recovery. Dispersion is affected by the spatial heterogeneity of porous media, the non-Newtonian behavior of polymer solutions, and the Brownian motion of nanoparticles. Here, we use the Euler-Lagrangian method to simulate the flow of nanoparticles and inelastic non-Newtonian fluids (described by Meter model) in a range of porous media samples and injection rates. In one case, we use a fine mesh of more than 3 million mesh points to model nanoparticles transport in a sandstone sample. The results show that the velocity distribution of nanoparticles in the porous medium is non-Gaussian, which leads to the non-Fickian behavior of nanoparticles dispersion. Due to pore-space confinement, the long-time mean-square displacement of nanoparticles depends nonlinearly on time. Additionally, the gradient of shear stress in the pore space of the porous medium dictates the transport behavior of nanoparticles in the porous medium. Furthermore, the Brownian motion of nanoparticles increases the dispersion of nanoparticles along the longitudinal and transverse direction.

I. INTRODUCTION

The migration and dispersion of nanoparticles in porous media are of considerable importance in various commercial, industrial, and natural systems [1–3]. The addition of nanoparticles in the polymer solution enhances the liquid's functional properties [4]. Therefore, the nanoparticles are widely used in various biological and industrial applications. For example, the use of nanoparticles to improve oil recovery has shown promising results for application in the field [5,6]. Nanoparticles in polymeric solutions improve the wetting properties of the pore surfaces [7], modify viscosity, reduce surface tension [8], control mobility, and has the potential to act as a catalyst [7]. Pore accessibility is an essential factor for nanoparticle transport in heterogeneous porous media, mainly in applications where nanoparticles are used as catalyst or property modifiers, e.g., soil remediation [9,10]. However, the fate and transport of nanoparticles within polymeric solutions at the pore scale are not fully understood due to the Brownian motion of nanoparticles and the non-Newtonian rheology of polymeric fluids.

Understanding the nanoparticle transport in porous materials is challenging due to multiple reasons. (i) The complex geometry of porous media, viz. voids accessibility, spatial structure, and connectivity govern nanoparticles' mobility in porous media [11]. (ii) Sizes of particles and pores affect the nanoparticles' dispersion [3,11,12]. (iii) Confinement in disordered porous media results in a non-Gaussian distribution of nanoparticle displacements [2]. (iv) Spatial and temporal variations in the fluid flow path affect the longitudinal and transverse displacement of nanoparticles. (v) The non-Newtonian shear-dependent rheology of the polymeric fluid further influences the migration and dispersion of nanoparticles in porous media [3,13]. Therefore, it is important to incorporate above-mentioned factors and distinguish different processes to elucidate the nanoparticle transport and dispersion in porous media under realistic conditions.

Advection and diffusion control dispersion of nanoparticles in heterogeneous porous media. Most studies of dispersion have focused on Newtonian fluids [11,14–23]. Few

_____

*masoud.babaei@manchester.ac.uk

studies in literature have evaluated the dispersion of nanoparticles in the longitudinal and transverse directions in porous media by tracking the movement of nanoparticles of non-Newtonian fluids. Scholz *et al.* observed a nonlinear increase in the dispersion coefficient of nanoparticles (size, 3 μm) in the polyacrylamide solution flowing in a square periodic array of obstacles [12]. They attributed the increase in dispersion with Weissenberg number to the cumulative effects of rheology-dependent velocity fluctuations arising from the periodic order in the medium. Babayekhorasani *et al.* [2] suggested that fluid rheology-dependent velocity fluctuations could be suppressed by random mixing in a heterogeneous porous medium compared to the ordered porous medium. In another work, Babayekhorasani *et al.* [24] reported that an increase in the confinement of porous medium decreases the diffusive mobility of nanoparticles in both Newtonian and non-Newtonian fluids due to hydrodynamic interactions. The pore-scale trajectories of nanoparticles motion tracked by Jacob *et al.* [3] showed that the elastic turbulence-based velocity fluctuations in hydrolysed polyacrylamide are higher in ordered porous media than they are in disordered porous media.

Using microfluidic experiments, Maitri *et al.* [25] found that nanoparticle channelization and distribution depend on the elasticity and Weissenberg number in ordered and disordered porous media. They suggested that a simplified structure may not always give a realistic overview of mass transport phenomena in a complex porous medium [25]. Finally, Aramideh *et al.* [26] used direct numerical simulation to investigate the dispersion of nanoparticles in a viscoelastic fluid. They observed that the elasticity did not alter the nanoparticles' long-term dispersion in viscoelastic fluids flowing through a 2D porous medium of a random array with a porosity of 40%. The viscoelasticity of non-Newtonian fluids lead to local velocity fluctuation during non-Newtonian fluid through porous media [27–31]. These chaotic velocity fluctuations significantly affect dispersion of nanoparticles in heterogeneous porous media [24,32].

A. This study

One can track the motion of individual particles at the pore scale to upscale the microscopic mass transport mechanisms and determine the macroscopic transport properties. This helps explain the pore-scale mass transport mechanism and provides representative macroscopic transport properties in the porous media. Although particle tracking in Newtonian fluids and 2D porous media has been extensively studied [11,33–35], there are no adequate investigation of nanoparticle transport in non-Newtonian fluids and 3D porous medium (with an exception of Refs. [2,24]).

The dependence of hydrodynamic interaction on dimensionality is different in 2D and 3D [36,37]. Therefore, it is not clear whether dispersion would be similar in 2D and 3D domains. Likewise, there are conflicting reports about the role of disorder in elastic fluctuations and dispersion in porous media (see Refs. [2,24] versus Ref. [12]). Previous research on nanoparticle tracking was primarily carried out at a significantly small domain in 2D due to instrumental limitations [2,3,12,38]. An exception to this is the work of

Refs. [24,39]. Furthermore, the porosity considered in these studies was considerably larger than the natural porous media. It is expected that reducing porosity and increasing heterogeneity will significantly alter dispersion. Previous studies on nanoparticle dispersion were carried out in a viscoelastic fluid [3,24]. Hence, it is pertinent to know how nanoparticles migrate in an inelastic fluid. Therefore, we simulated nanoparticle transport of an inelastic non-Newtonian fluid flowing through a converging-diverging microchannel in 3D, homogeneous ordered 2D porous medium, and Mt. Simon sandstone in 3D over a range of injection rates. The objectives of the present work include:

(i) developing an Eulerian-Lagrangian framework to simulate nanoparticle transport within non-Newtonian fluid and 3D porous media incorporating particle-fluid, particle-particle, particle-wall interactions, and Brownian motion;

(ii) evaluating pore-accessibility of nanoparticles in heterogeneous domains;

(iii) determining dispersion coefficient along transverse and longitudinal direction over a range of fluid injection rates and porous media geometries.

This study aims to make two new contributions. To our knowledge, there is no 3D pore-scale two-phase simulation study that incorporates nanoparticles as a distinct phase (using the Euler-Lagrangian method) during an inelastic non-Newtonian fluid flow in a real 3D heterogeneous porous medium, which is the first contribution of the work. Second, contrary to the results in the literature [40,41], our results show anomalous behavior of nanoparticle dispersion in both homogeneous and heterogeneous porous media during flow in a Newtonian and an inelastic non-Newtonian fluid over a range of Péclet numbers. In addition, we have also shown that the gradient of shear stress formed during fluid flow modulates the migration of nanoparticles in porous media.

II. GOVERNING EQUATIONS

To investigate nanoparticle transport in a polymeric non-Newtonian fluid, we use the Eulerian-Lagrangian approach. In this approach nanoparticles are treated as suspended in the solution. We solve governing equations of the inelastic Meter model fluid. The nanoparticle motions are predicted based on the previously calculated flow field and Newton's second law at each time step. We use an OpenFOAM C++ library to perform Eulerian-Lagrangian-based particle-fluid simulations.

A. Eulerian frame

We describe the single-phase, laminar flow of non-Newtonian fluids using continuity [Eq. (1)] and momentum [Eq. (2)] equations,

$$\nabla \cdot \mathbf{u}_{\mathrm{f}} = 0, \tag{1}$$

$$\rho_{\mathrm{f}}\left(\frac{\partial \mathbf{u}_{\mathrm{f}}}{\partial t} + \mathbf{u}_{\mathrm{f}} \cdot \nabla \mathbf{u}_{\mathrm{f}}\right) = -\nabla P + \nabla \cdot \boldsymbol{\tau} - \mathbf{S}_{\mathrm{p}}, \tag{2}$$

where ρ_{f} [kg/m^3] is the density of fluid, $\mathbf{u}_{\mathrm{f}}$ [m/s] is the velocity vector of fluid phase, P [Pa] is pressure, t [s] is time, $\boldsymbol{\tau}$ [Pa] is the fluid stress tensor, and $\mathbf{S}_{\mathrm{p}}$ is an additional source term that considers the effect of particle forces on the fluid

motion at each time step. The constitutive equation of the inelastic stress-dependent Meter model is defined as [42–44]

$$\boldsymbol{\tau} = 2\,\eta(\tau)\,\mathbf{D} = \eta(\tau)\left[\nabla\mathbf{u}_\mathrm{f} + (\nabla\mathbf{u}_\mathrm{f})^T\right]. \quad (3)$$

In the present work we use Meter model [Eq. (4)], which describes S-shaped rheology of most of the shear thinning and shear thickening fluids. This model describes the stress dependence of the shear viscosity as [42–44]

$$\eta = \eta_\infty + \frac{\eta_0 - \eta_\infty}{1 + \left(\frac{\tau}{\tau_m}\right)^S}, \quad (4)$$

where η [Pa s] is the shear viscosity at a given shear stress, η_0 [Pa s] is the zero-shear viscosity, η_∞ [Pa s] is an infinite shear viscosity, τ_m [Pa] is the critical shear stress parameter, and S is an exponent representing slope.

B. Lagrangian frame

Particles interact with each other, with the wall, and with the surrounding fluid while migrating in the porous medium. The Discrete Element Model (DEM) can be used to solve the governing equations of particle motion [45–47] in porous media. Newton's second law governs the motion of the particles in the Lagrangian framework [Eq. (5)] [45,46,48]

$$m_\mathrm{p}\frac{d\mathbf{u}_\mathrm{p}}{dt} = \mathbf{F} = \mathbf{F}_\mathrm{C} + \mathbf{F}_\mathrm{F}, \quad (5)$$

where m_p (kg) is the particle mass, $\mathbf{u}_\mathrm{p}$ (m/s) is the particle velocity, $\mathbf{F}$ is the total forces acting on particles, $\mathbf{F}_\mathrm{C}$ is the contact forces acting on the particles due to interparticle interaction or particle-wall interactions, and $\mathbf{F}_\mathrm{F}$ is the particle-fluid interaction forces acting on particles. Readers are referred to Ref. [46] for details on the implementation of DEM in OpenFOAM.

1. Particle-fluid interaction

Several particle-fluid interaction forces can act on the particle during its migration in the fluid [36]. In the present work, we defined particle-fluid forces as

$$\mathbf{F}_\mathrm{F} = \mathbf{F}_\mathrm{D} + \mathbf{F}_{\mathrm{G,B}} + \mathbf{F}_\mathrm{P} + \mathbf{F}_\mathrm{B}, \quad (6)$$

where $\mathbf{F}_\mathrm{D}, \mathbf{F}_{\mathrm{G,B}}, \mathbf{F}_\mathrm{P}, \mathbf{F}_\mathrm{B}$ are the drag force, combined gravity and buoyancy force, pressure force, and Brownian motion forces acting on the particle, respectively. The drag force ($\mathbf{F}_\mathrm{D}$) acting on the particle is given by

$$\mathbf{F}_\mathrm{D} = \frac{3\,C_d\,\mathrm{Re}_\mathrm{p}\,m_\mathrm{p}\,\eta\,(\mathbf{u}_\mathrm{f} - \mathbf{u}_\mathrm{p})}{4\,\rho_\mathrm{p}\,d_\mathrm{p}^2}, \quad (7)$$

where C_d is the drag coefficient, Re_p is the particle Reynolds number, ρ_p [kg/m³] is the density of the particle, and d_p [m] is the diameter of the particle. The Reynolds number of particles in the flow is below 10 in the present work, thus, $C_d\,\mathrm{Re}_\mathrm{p} = 24\,(1 + \frac{1}{6}\mathrm{Re}_\mathrm{p}^{2/3})$ [46]. The combined buoyancy and gravity forces ($\mathbf{F}_{\mathrm{G,B}}$) due to gravity g [m/s²] and the force act on the particle due to local pressure gradient ($\mathbf{F}_\mathrm{P}$) are estimated as [46]

$$\mathbf{F}_{\mathrm{G,B}} = m_\mathrm{p}\,g\left(1 - \frac{\rho_\mathrm{f}}{\rho_\mathrm{p}}\right), \quad (8)$$

$$\mathbf{F}_\mathrm{P} = \frac{\pi\,d_\mathrm{p}^3}{6}\Delta P. \quad (9)$$

Nanoparticles exhibit Brownian motion, which is expected to strongly affect their dispersion in a porous medium. Thus, we implemented the Brownian force ($\mathbf{F}_\mathrm{B}$) as a Gaussian white noise random process following Lee and Ahmadi [49] as

$$\mathbf{F}_\mathrm{B} = \xi_\mathrm{i}\left(\frac{\pi}{\Delta t}\delta_{\mathrm{ij}}\frac{216\,\nu\,k_\mathrm{B}\,T}{\pi^2\,d_\mathrm{p}^5\,\rho_\mathrm{f}\,C_\mathrm{c}\left(\frac{\rho_\mathrm{p}}{\rho_\mathrm{f}}\right)^2}\right)^{\frac{1}{2}}, \quad (10)$$

where ξ_i is the Gaussian random number with zero mean and unit variance, Δt is the time step, δ_{ij} is the Kronecker δ function, k_B (J/K) is the Boltzmann constant, T (K) is the temperature, ν (m²/s) is the kinematic viscosity, and C_c is the Stokes-Cunningham slip correction, which is a function of the molecular mean free path (λ_m), given as

$$C_\mathrm{c} = 1 + \frac{2\lambda_\mathrm{m}}{d_\mathrm{p}}\left(1.257 + 0.4e^{\dfrac{1.1d_\mathrm{p}}{2\lambda_\mathrm{m}}}\right). \quad (11)$$

2. Particle contact forces

We use a simple spring-slider-dashpot model implemented in OpenFOAM to determine contact forces due to particle collisions. The dashpot represents viscous dissipation, whereas the spring represents elastic deformation. This model uses the Hertzian contact theory [48]. Readers are referred to Refs. [46,48,50–52] for a detailed description of particle contact forces. In summary, the force $\mathbf{F}_{\mathrm{p,ij}}$ acting during collision between two particles i and j is divided into normal ($\mathbf{F}_{\mathrm{n,ij}}$) and tangential ($\mathbf{F}_{\mathrm{t,ij}}$) components and is given as

$$\mathbf{F}_{\mathrm{p,ij}} = \mathbf{F}_{\mathrm{n,ij}} + \mathbf{F}_{\mathrm{t,ij}} = \left(k_\mathrm{n}\delta_\mathrm{n}^b + \gamma_\mathrm{n}\nu_\mathrm{n}\right) + (k_\mathrm{t}\delta_\mathrm{t} + \gamma_\mathrm{t}\nu_\mathrm{t}), \quad (12)$$

where k_n and k_t are stiffness coefficients in the normal and tangential directions of particles, δ_n and δ_t are normal and tangential displacements due to particle-particle interactions, $b = 1.5$ is a collision constant, γ_n and γ_t are normal and tangential viscous damping constants, and ν_n and ν_t are the relative velocities between particles in normal and tangential directions. Similarly, the force $\mathbf{F}_{\mathrm{w,i}}$ acting during a collision between particle i and wall w is decomposed into normal $\mathbf{F}_{\mathrm{n,wi}}$ and tangential $\mathbf{F}_{\mathrm{t,wi}}$ parts and are calculated as

$$\mathbf{F}_{\mathrm{w,i}} = \mathbf{F}_{\mathrm{n,wi}} + \mathbf{F}_{\mathrm{t,wi}} = \left(k_{\mathrm{nw}}\delta_{\mathrm{nw}}^b + \gamma_{\mathrm{nw}}\nu_{\mathrm{nw}}\right) \\ + (k_{\mathrm{tw}}\delta_{\mathrm{tw}} + \gamma_{\mathrm{tw}}\nu_{\mathrm{tw}}), \quad (13)$$

where k_{nw} and k_{tw} are stiffness coefficients in the normal and tangential direction of the particles-wall interaction, respectively. δ_{nw} and δ_{tw} are normal and tangential displacements due to the particle-wall interactions, respectively. γ_{nw} and γ_{tw} are normal and tangential viscous damping constants for the particle-wall interactions, respectively. ν_{nw} and ν_{tw} are the relative velocities between particle and wall in normal and tangential directions, respectively. The total force acting on the particle due to particle-particle and particle-wall interaction will be as

$$\mathbf{F}_\mathrm{C} = \mathbf{F}_{\mathrm{p,ij}} + \mathbf{F}_{\mathrm{w,i}}. \quad (14)$$
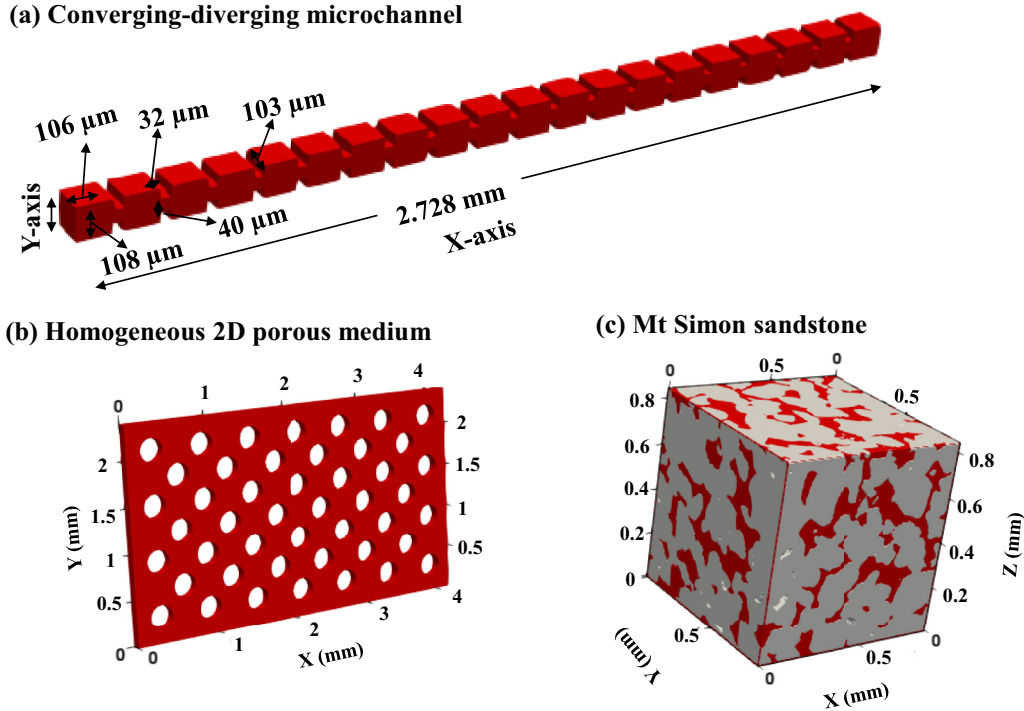
FIG. 1. Geometry of (a) symmetric converging-diverging microchannel with 20 repetitive elements (3D), (b) homogeneous ordered porous medium (2D), and (c) Mt. Simon sandstone (3D). Red indicates pore spaces. Fluid flows along positive *x* direction.

C. Numerical scheme and the solver

The DPMFoam solver is a discrete particle modeling solver of OpenFOAM, designed to couple Eulerian and Lagrangian frames. A detailed description of the DPMFoam is presented in Ref. [46]. We modified the DPMFoam solver of OpenFOAM to implement the Meter model. For simulating inelastic Meter model fluid, we used backward scheme to discretize time, Gauss linear upwind to discretize divergence, Gauss linear scheme to discretize gradient, and Gauss-linear corrected scheme to discretize the Laplacian term. PIMPLE algorithm was used for pressure-velocity coupling [53,54]. We used the Euler scheme to integrate velocity during Lagrangian particle transport. The computationally expensive simulations were carried out in parallel in the high performance computing cluster facility of the University of Manchester.

D. Numerical domain and boundary conditions

We simulated nanoparticle transport (d_p of 400 nm) in 3D converging-diverging microchannel having 20 repetitive elements, in a 2D homogeneous porous medium having porosity of 70%, and in 3D Mt. Simon sandstone of Ref. [55] having porosity of 24%, as shown in Fig. 1. The pore-sizes of microchannel, homogeneous medium, and sandstone ranged from 32–108 μm, 150 μm, and 2–100 μm, respectively. The degree of anisotropy of sandstone is 0.255, whereas microchannel and homogeneous 2D porous medium are isotropic.

No-slip velocity and zero fixed flux pressure boundary conditions were applied at front, back, top, bottom, and solid surfaces of 3D domain. Zero flux corrected velocity and total pressure boundary conditions were applied to the right boundary (outlet) of the porous medium domain. Constant injection velocity boundary condition was applied at the inlet (left boundary) of the porous medium. We injected 500 (unless otherwise noted) polystyrene nanoparticles per second for 1 s at the inlet (left boundary) during numerical experiments. The polystyrene nanoparticle had a density of 1050 kg/m^3, a Young modulus of 1.25×10^9 N/m^2, and a Poisson's ratio of 0.33. For Brownian motion force calculation, we fixed the temperature of the polymeric solution at 300 K and the mean free path of the particle in the polymeric solution as 1×10^{-9} m. Polyacrylamide solution [56,57] is a commonly employed polymeric solution for enhanced oil recovery applications [58–60]. Thus, we investigated the transport of nanoparticles in 0.125% polyacrylamide (PAA) fluid having density of 1300 kg/m^3 of Ref. [3]. The Meter model parameters of PAA are $\eta_0 = 2.1$ Pa s, $\eta_\infty = 0.001$ Pa s, $\tau_m = 0.3$ Pa, and $S = 1.8$ [3]. We simulated the flow of polymeric non-Newtonian fluid and Newtonian fluid ($\eta = 2.1$ Pa s) over a range of injection rates. The Courant number $C = \frac{u\Delta t}{\Delta x}$, where Δt is the timestep and Δx is the length interval, was maintained below 0.9 in all simulations. A fine mesh of more than 3 million mesh points were generated in the pore space of porous medium using snappyHexMesh module of OpenFOAM. The volume fraction of the nanoparticles was lower than 0.005 during all simulations, which implies that the system is dilute and particle interaction was limited. The *rebound* module of OpenFOAM was used to consider the aggregation of nanoparticle particles and the adsorption of nanoparticles at porous media boundaries. During the simulation, the coefficient of restitution (*e*) was 0.95 [45,46,48], which implies a real-world inelastic collision between nanoparticles. The

particles were randomly distributed in the inlet plane at the start of the numerical experiments to evaluate the effect of random particle distribution at the inlet on dispersion. The spatial distribution of nanoparticles at the inlet was significantly different at each Péclet number, as we injected a constant number of nanoparticles per second.

III. NANOPARTICLE TRAJECTORY ANALYSIS

The mean-square displacement (MSD) of the nanoparticles as a function of a lag time (t') in a porous medium was calculated as [11]

$$\text{MSD}(t') = \langle \mathbf{r}(t')^2 \rangle = \langle [\mathbf{r}(t + t') - \mathbf{r}(t')]^2 \rangle, \quad (15)$$

where $\mathbf{r}(t)$ is position of nanoparticles in porous medium at time t, and $\langle \rangle$ indicates an ensemble or time-averaged value. The MSD was fitted to $\langle r(t')^2 \rangle = 2D_{L,T} t'$ to determine dispersion coefficient [61]. In addition, using the particle velocity data, we calculated longitudinal (D_L, along flow direction) or transverse (D_T, normal to flow direction) dispersion coefficients using Eq. (16) [3,62]:

$$D_{L,T} = \frac{1}{2} \frac{d\sigma_{L,T}^2}{dt^2} = \int C_{L,T}(t') \, dt', \quad (16)$$

where $C_{L,T}(t') = \langle [v_{x,y}(t + t') - \langle v_{x,y} \rangle][v_{x,y}(t) - \langle v_{x,y} \rangle] \rangle$ is the autocorrelation of velocity $v_{x,y}(t')$, and $\sigma_{L,T}^2(t)$ which is the second moment of the particle displacement in a longitudinal or transverse direction. Here, $v_{x,y}(t)$ and $v_{x,y}(t + t')$ are the longitudinal and transverse velocity of a particle at the start of trajectory and after a lag time t', respectively; and $\langle v_{x,y} \rangle$ is the average velocity of particles over all time and trajectories [3,62]. The Stokes-Einstein equation was used to determine the molecular diffusion coefficient of spherical nanoparticles in a non-Newtonian fluid [61],

$$D_{SE} = \frac{k_B T}{3\pi \, \eta_0 \, d_p}, \quad (17)$$

where D_{SE} [m^2/s] is the Stokes-Einstein-based molecular diffusion coefficient. The dispersion coefficient was normalized by D_{SE}. We define the relative variation in the rate of advection and diffusion using Péclet number (Pe), and the relative variation of inertial forces and viscous forces using Reynolds number (Re) following

$$\text{Pe} = \frac{U_{avg} \, \delta_L}{D_{SE}}, \quad (18)$$

$$\text{Re} = \frac{\rho_f \, U_{avg} \, \delta_L}{\eta_{eff}}. \quad (19)$$

Here, U_{avg} (m/s) is the average pore-scale velocity of the fluid, η_{eff} (Pa s) is the effective viscosity of the fluid flow, and δ_L (m) is the characteristic length scale. The velocity, viscosity, shear rate, and pore size vary spatially in the porous medium; thus, to estimate the representative dimensionless number of the fluid flow in the porous medium, we use volume-averaged values of velocity, viscosity, and shear rate. We integrate the pore-scale velocity, shear rate, shear stress, and viscosity over a pore space filled with polymeric non-Newtonian fluids to determine the volume-averaged velocity (U_{avg}), volume-averaged shear rate ($\dot{\gamma}_{avg}$), volume-averaged

shear stress (τ_{avg}), and volume-averaged effective viscosity (η_{eff}) [44]. The dimensionless time is defined as

$$t_D = \frac{t \, U_{avg}}{\delta_L}. \quad (20)$$

IV. ASSUMPTIONS AND LIMITATIONS

Most non-Newtonian fluids show viscoelastic properties (e.g., relaxation time, normal stress, extensional viscosity, and shear modulus). However, the rheology of non-Newtonian fluids has been studied in the past by looking at the flow as either a generalized Newtonian fluid (like power-law, Bingham, Cross, Carreau, Elis, and Meter models) or a viscoelastic fluid (like Maxwell, Oldroyd-B [63], Giesekus [64], Phan-Thien-Tanner [65], and Bautista-Manero [66] models). These models were created using an empirical approach with several simplified assumptions [67]. As a result, each model has its own limitations and cannot be applied to all types of non-Newtonian fluids. In the present paper, we used the Meter model [42], which is an empirical equation that fits the shear viscosity-shear stress data of most shear thinning as well as shear thickening fluids. Please see our recent work [43,44,68,69] for more details on the Meter model. The fluids' viscoelasticity is not taken into account by the Meter model equation. As a result, the impact of elastic turbulence-based velocity fluctuations on nanoparticle transport is overlooked in this study. The Euler method-based viscoelastic fluid flow simulations have numerical stability issues [50,70,71]. Furthermore, there is still a challenge to coupling Euler method-based viscoelastic models with a Lagrangian framework. Readers are referred to Refs. [67,70–72] for detailed information on the assumptions and limitations of GNF and viscoelastic fluid flow simulations. These models provide some understanding of the fluid dynamics of non-Newtonian fluids, despite the fact that they are based on specific assumptions and have limits.

V. RESULTS AND DISCUSSION

A. Homogeneous porous medium

Tracking nanoparticle transport in 3D provides insight into transport in real (or practical) settings compared to 2D. Therefore, we simulated the flow of nanoparticles in Newtonian and inelastic non-Newtonian fluids and in 3D converging-diverging microchannel over a range of Pe (10^6–10^8). Figure 2 and movie S1 of the Supplemental Material [73] show nanoparticle transport behavior in Newtonian and non-Newtonian fluids at Pe of 2.48×10^6. Although fluid flow velocity is low (i.e., 10^{-4} m/s), nanoparticles show channelized motion along a flow direction with time in both Newtonian and non-Newtonian fluids. Movie S1 of the Supplemental Material [73] shows that the spatial distribution of nanoparticles after 2 s is relatively dense compared to the spatial distribution at 5 and 10 s in both Newtonian and non-Newtonian fluids. The local spatial density of particles at 2 s was 1.72×10^5 particles/mm^3, whereas spatial density of particles at 10 s were 1.44×10^4 particles/mm^3. This is expected as there is axial dispersion even in straight
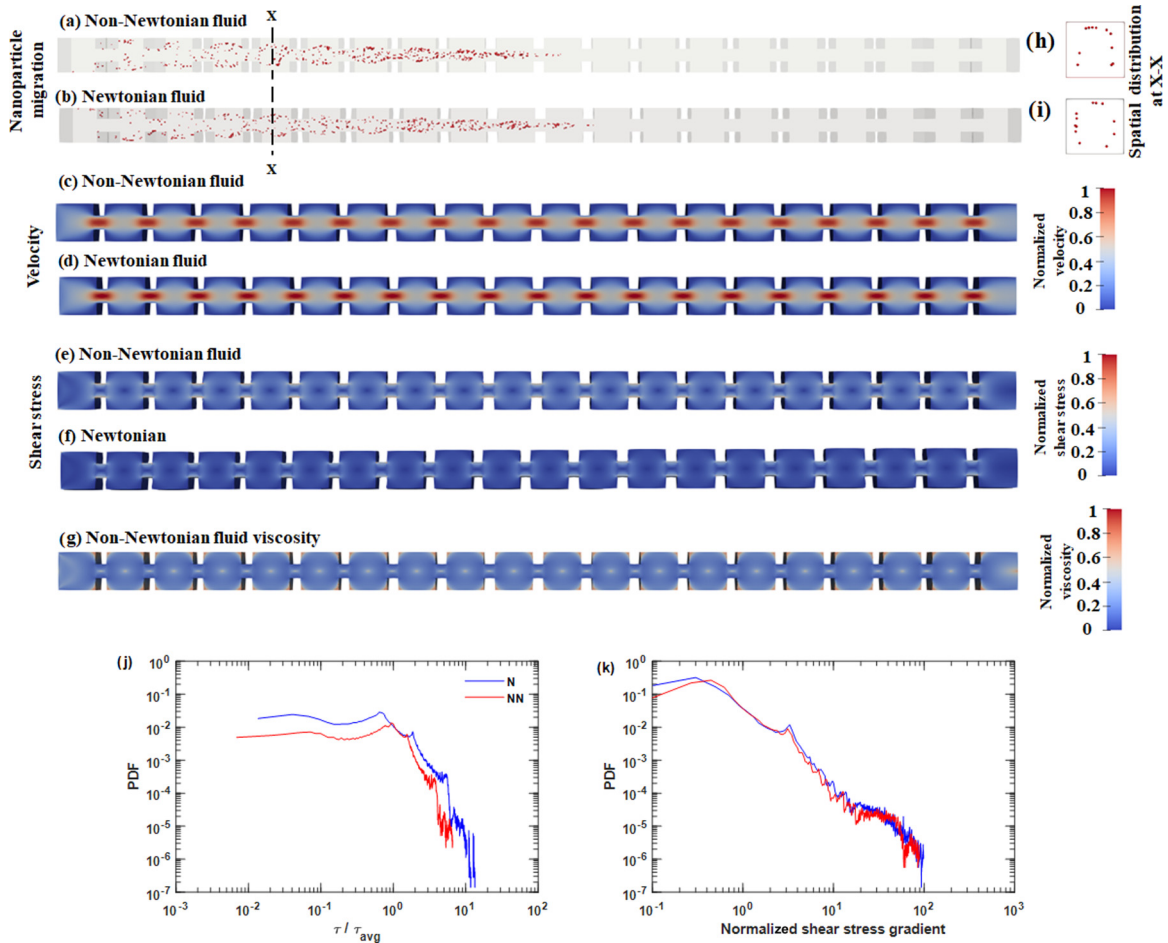
FIG. 2. Spatial distribution of nanoparticles at $t_D = 12$ in converging-diverging microchannel: (a) with non-Newtonian fluid and (b) Newtonian fluid at Pe $= 2.48 \times 10^6$. Spatial distribution of (c), (d) velocity, (e), (f) shear stress, and (g) viscosity at the middle section of the microchannel. The spatial distribution of nanoparticles at section x-x: (h) non-Newtonian fluid and (i) Newtonian fluid. (j), (k) Probability density function (PDF) of normalized shear stress and normalized shear stress gradient in Newtonian (N) and non-Newtonian (NN) fluids. Shear stress and shear stress gradient are normalized using average value.

channels. This also suggests that converging-diverging geometry influenced the dispersion of nanoparticles.

The velocity of the nanoparticles depended on the spatial location of particles. The particles at the center had high velocity, whereas particles near boundaries had much lower velocity. Figures 2(c)–2(g) show a spatial profile of the velocity, shear stress and viscosity of the non-Newtonian fluid and Newtonian fluid at the center of the microchannel. Figures 2(e) and 2(f) depict that shear stress at the corner and center of the channel is minimum in both Newtonian and non-Newtonian fluids. This spatial distribution of shear stress imparts resistance for the transport of nanoparticles in those regions, which slows down the velocity of nanoparticles trapped at a corner. Figures 2(e) and 2(f) show that shear stress at the center of the microchannel is minimum, and the gradient of shear stress initially increases and then decreases spatially from the center toward outer boundaries in both converging and diverging regions of the microchannel. This spatial distribution of shear stress of fluid flow governs the location of nanoparticles during their transport. Figures 2(h) and 2(i) show that most nanoparticles avoided the regions with lower shear stress, i.e., the center of the microchannel. Therefore,

most nanoparticles were mostly channelized toward equilibrium position, i.e., in the region with maximum shear stress. This result agrees with channelization of nanoparticles in non-Newtonian fluids reported by Refs. [74–77]. Figures 2(e) and 2(f) show distinct difference in shear stress distributions between the non-Newtonian fluid and the Newtonian fluid due to spatial variation of viscosity in a non-Newtonian fluid [see Fig. 2(g)]. The probability density function (PDF) of normalized shear stress and normalized shear stress gradient of Newtonian and inelastic non-Newtonian fluid shows significant difference [see Figs. 2(j) and 2(k)]. This result imply that the slight spatiotemporal variation in nanoparticle distribution in Newtonian and non-Newtonian fluids at the same Pe is due to spatial viscosity and shear stress variations.

Figure 3 shows the spatial distribution of nanoparticles at $t_D = 2$, and 7 in Newtonian and inelastic non-Newtonian fluids in the 2D homogeneous porous medium at Pe of 1.13×10^6. These results indicate that nanoparticles follow a similar channelized flow path and but slightly different spatiotemporal distribution in both Newtonian and non-Newtonian fluids. The slight variation of resident concentration of nanoparticles [Fig. 3(e)] in both Newtonian and
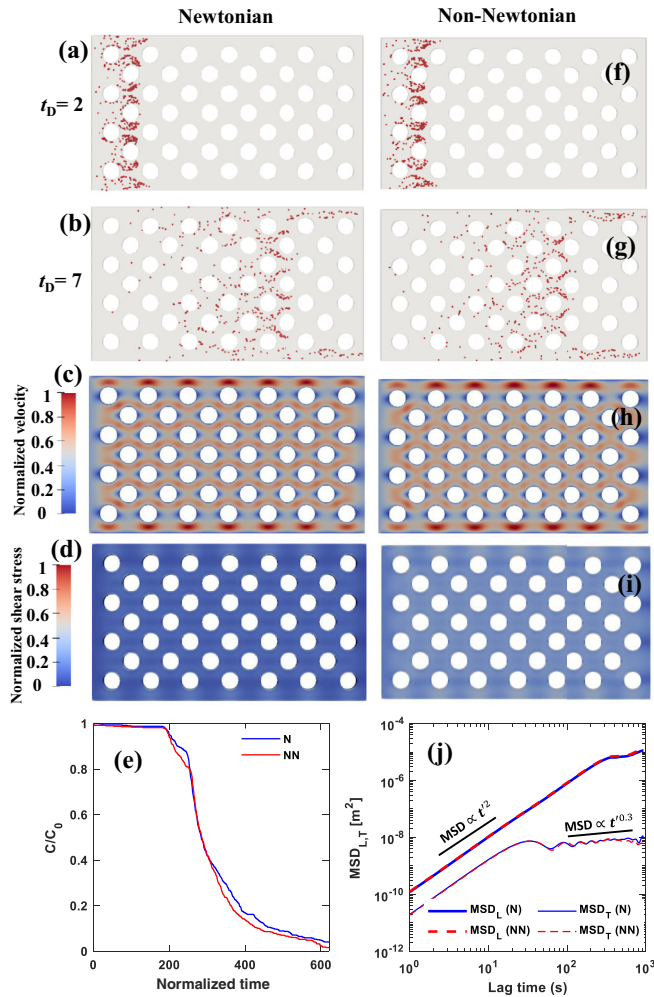
FIG. 3. (a), (f) Spatial distribution of nanoparticles at $t_D = 2$, (b), (g) at $t_D = 7$. (c), (h) Normalized velocity of fluid and (d, i) normalized shear stress in 2D homogeneous porous medium in Newtonian (N) and non-Newtonian (NN) fluids. (e) Normalized concentration of nanoparticles in the porous medium as a function of dimensionless time (t_D). (j) Mean-square displacement (MSD) along longitudinal direction and transverse direction (Pe = 1.13×10^6). Black line shows that short time MSD is function of t'^2 indicating superdiffusive dispersion and long time transverse MSD is function of $t'^{0.3}$ indicating subdiffusive dispersion.

non-Newtonian fluids is due to the shear-thinning property of non-Newtonian fluids. The non-Newtonian curve is not consistently on one side of the Newtonian curve in Fig. 3(e). Figure 3(j) shows an overlap of MSD profile along longitudinal and transverse direction for both Newtonian and non-Newtonian fluids. These results imply that the dispersion of nanoparticles in an inelastic non-Newtonian fluid is not significantly affected by inelastic shear thinning nature of the non-Newtonian fluid in a 2D homogeneous porous media of porosity 70%.

Figure 3(j) shows that nanoparticles follows anomalous dispersion. Nanoparticle dispersion deviates from a linear relationship and adopted an asymptotic form of MSD $\propto t'^{\alpha}$, here α is the anomalous dispersion exponent [78,79], $\alpha = 1$ indicates Fickian dispersion, $\alpha < 1$ indicates subdiffu-

sive dispersion, and $\alpha > 1$ indicates superdiffusive dispersion [11,78]. Figure 3 shows that MSD $\propto t'^2$, which corresponds to non-Fickian ballistic superdiffusive dispersion process at short time [11,19,78,79]. MSD $\propto t'^{0.3}$ along transverse direction implies that nanoparticles follows subdiffusive process at long time. Furthermore, we were not able to fit the analytical solution of the advection-dispersion equation (Fickian transport) in Fig. 3(e) to estimate the dispersion coefficient. These results indicate that nanoparticles transport is non-Fickian and this likely arises from the strong confinement for both Newtonian and inelastic non-Newtonian fluids. The overlap of the MSD curves of Newtonian and non-Newtonian fluids in Fig. 3(j) means that the rheology of inelastic fluids does not play an important role in the non-Fickian behavior of nanoparticles transport in homogeneous 2D porous media.

B. Mt. Simon sandstone

Figure 4 depicts the spatial distribution of nanoparticles at dimensionless time of 6 and 45 in Newtonian and inelastic non-Newtonian fluids at Pe of 1.26×10^6 along with spatial distribution of shear stress gradient in the Mt. Simon sandstone. Movies S2, S3, and S4 of the Supplemental Material [73] show nanoparticle transport behavior in Mt. Simon sandstone at Pe of 1.26×10^6, 2.51×10^7, and 1.26×10^8, respectively. At Pe of 1.26×10^6, the spatial distribution of nanoparticles is scattered [Figs. 4(a) and 4(b)]; on the contrary, due to the channelled migration of nanoparticles, this scattered distribution was not observed at higher Pe (i.e., 1.26×10^7 and 1.26×10^8). Furthermore, there are drastic spatial variations of shear stress gradient values in sandstone for Newtonian and non-Newtonian fluids [Figs. 4(c) and 4(f)]. Figure 4(g) shows that normalized shear stress distributions in Newtonian and non-Newtonian fluid over a range of Pe are different. Similarly, normalized *gradient* of shear stress in Newtonian and non-Newtonian also show significant difference in the order of values [Fig. 4(h)] over a range of Pe.

The local shear stress gradient governs the spatiotemporal distribution of nanoparticles in Newtonian and non-Newtonian fluids. Figures 4(g) and 4(h) indicate that the probability density function (PDF) of distribution normalized shear stress and normalized shear stress gradient of Newtonian and non-Newtonian fluid is significantly different. The normalized shear stress PDF curve during non-Newtonian fluid flow shows a flat region at low shear stress values, whereas Newtonian fluid flow shows a continuously decreasing profile. The flat region of the normalized shear stress PDF curve of non-Newtonian fluid in Fig. 4(g) indicates that a large portion of sandstone has low shear stress values during non-Newtonian fluid flow as compared to the Newtonian fluid flow. Furthermore, the shear stress gradient PDF of Newtonian fluid is higher than non-Newtonian fluids PDF [see Fig. 4(h)]. These results indicate that Newtonian fluid flow has more regions with high shear stress values and high shear stress gradients as compared to the non-Newtonian fluid flow. The transport of nanoparticles in the high-shear stress zone is much stronger compared to the low-shear stress zone. Thus, the dispersion of nanoparticles in a Newtonian fluid is expected to be more as compared to the dispersion in non-Newtonian fluid in sandstone.
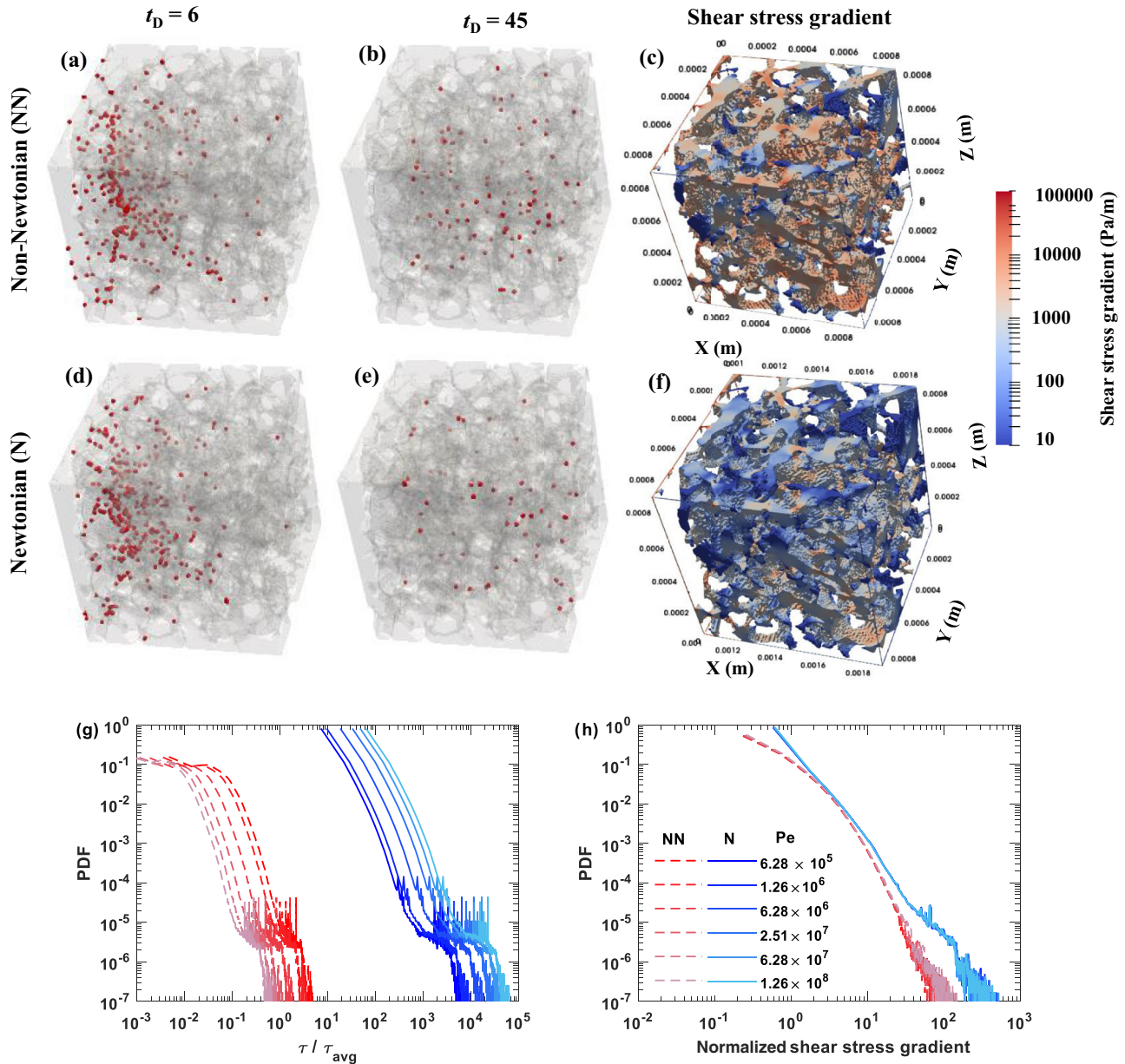
FIG. 4. Spatial distribution of nanoparticles in Mt. Simon sandstone at normalized time (t_D) 6 and 45 and spatial distribution of shear stress gradient at Péclet number 1.26×10^6 in Newtonian and non-Newtonian fluids. (g), (h) Probability density function (PDF) of normalized shear stress (τ/τ_{avg}) and normalized shear stress gradient in Newtonian (N) and non-Newtonian (NN) fluids over range of Péclet number. Size of nanoparticles in the images were enlarged for visibility. Shear stress and shear stress gradient is normalized using average value.

To evaluate further, we segmented pore space of sandstone into immobile and mobile regions. The immobile regions are defined as regions in which fluid velocity is 3 orders of magnitude lower than the average velocity [44]. Figure 5 shows immobile regions during Newtonian and inelastic non-Newtonian fluid flow at Pe of 6.28×10^7 along with spatial distribution of nanoparticles at t_D of 12. 22% and 25% of pore-space regions of sandstone were immobile during Newtonian and non-Newtonian fluid flow at Pe of 6.28×10^7, and large portion of immobile zones were dead-end zones of sandstone. Likewise, we observed that channelized fluid transport at Pe $> 10^7$ in the heterogeneous porous medium leads to a slightly higher stagnant/immobile region in the non-Newtonian fluid than the Newtonian fluid.

We evaluated nanoparticle dispersion using the mean-square displacement and velocity autocorrelation function approach [2,3,12,24,26]. Figures 6(a) and 6(b) show that MSD is a nonlinear function of lag-time along longitudinal and transverse directions in the Mt. Simon sandstone over a range of Péclet numbers. Figures 6(a) and 6(b) indicate that the difference between Newtonian and non-Newtonian for MSD curves increases for higher lag-times. Figures 6(a) and 6(b) show that short time $\mathrm{MSD}_{L,T} \propto t'^{1.7}$, whereas long time $\mathrm{MSD}_{L,T} \propto t'^{0.3}$ over a range of Pe. These results suggest that nanoparticles shows non-Fickian superdiffusive dispersion process at short time whereas it shows non-Fickian subdiffusive dispersion process along longitudinal as well as transverse direction at long time [11,19,78,79].

(a) Newtonian   **(b) Non-Newtonian**   **(c) Difference in immobile region**
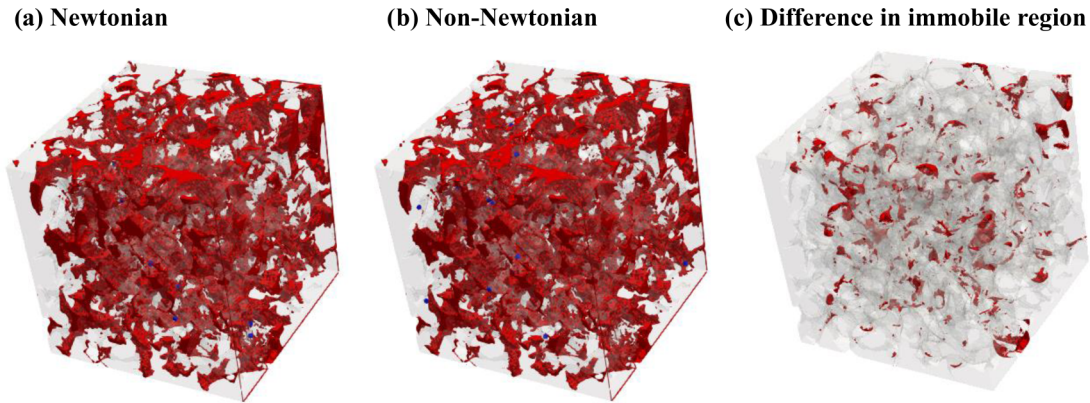
FIG. 5. Spatial distribution of immobile/stagnant regions (in red) and nanoparticles (in blue) in a Mt. Simon sandstone during flow of (a) Newtonian fluid, and (b) inelastic non-Newtonian fluid at Pe of 6.28×10^7 and at $t_D = 12$. (c) Difference between immobile region during Newtonian and inelastic non-Newtonian fluid flow. Pore space of 22% and 25% was immobile during Newtonian and non-Newtonian flow, respectively.

Figure 6(c) shows that D_L and D_T of Newtonian and non-Newtonian fluids increase linearly with increase in Pe. However, D_L and D_T of Newtonian fluid are consistently higher than non-Newtonian fluid. Two-sample statistical T test had a p value of 0.23-0.62 for Pe less than 10^7, indicating an insignificant difference in dispersion coefficient for Newtonian and non-Newtonian fluids at Pe $<10^7$. The

p value of 0.007–0.04 at Pe higher than 10^7 indicates a significant difference in dispersion coefficient for Newtonian and non-Newtonian fluids. The long-time MSD at Pe higher than 10^7 in Figs. 6(a) and 6(b) shows the significant difference in MSD curve for Newtonian and non-Newtonian fluids. This difference arises due to spatiotemporal difference in shear stress distribution in Newtonian and non-Newtonian
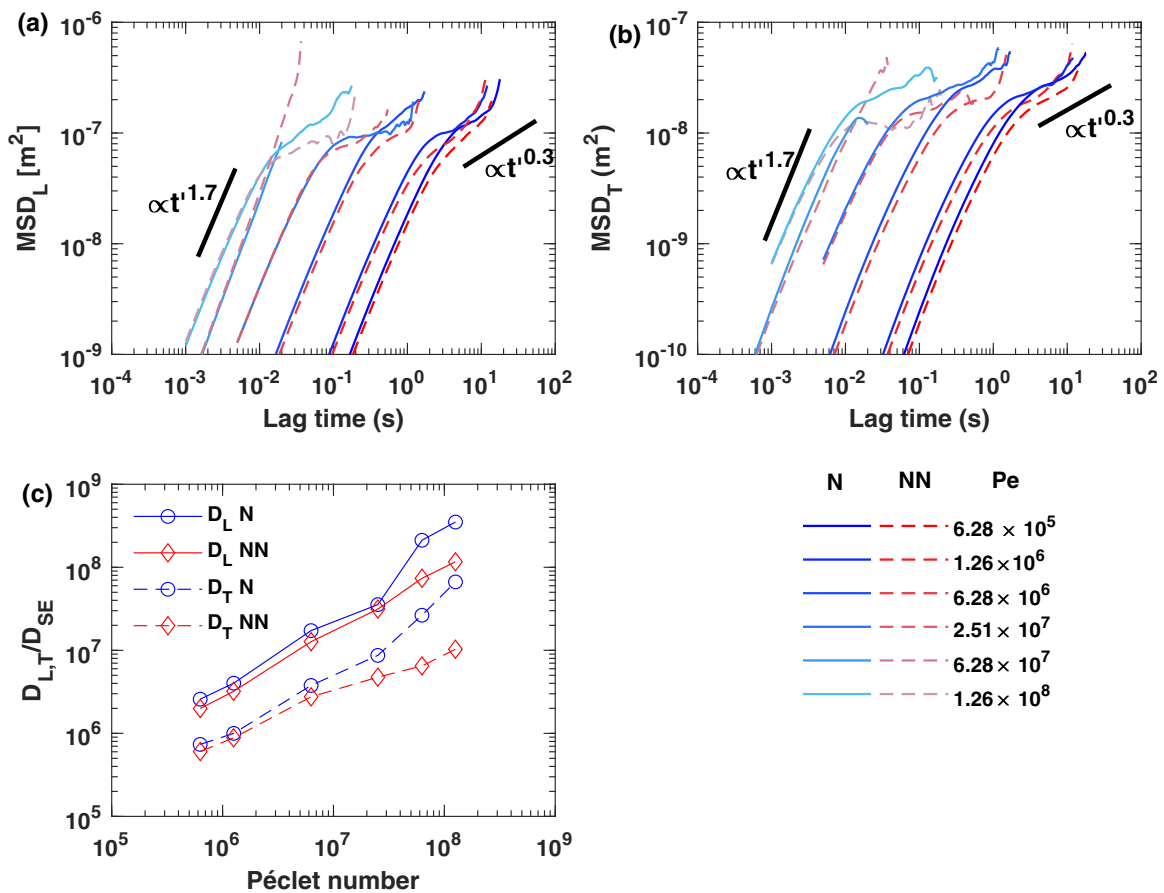

FIG. 6. Mean-square displacement (MSD) along (a) longitudinal direction, (b) transverse direction, and (c) normalized longitudinal and transverse dispersion coefficients over a range of Péclet numbers in Newtonian (N) and non-Newtonian (NN) fluids and Mt. Simon sandstone.
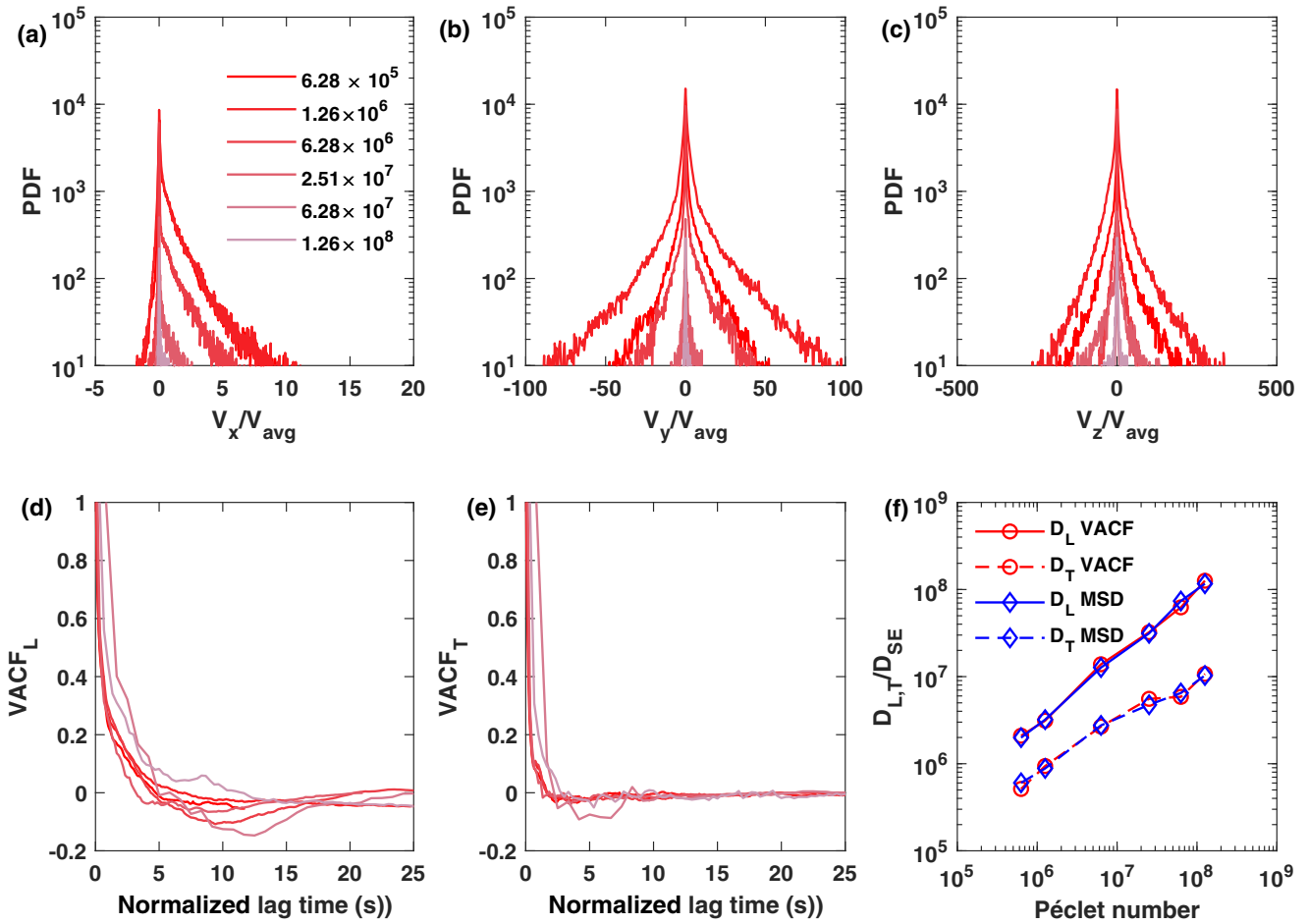
FIG. 7. Probability density function (PDF) of nanoparticle velocity along (a) longitudinal X-direction, (b) transverse y direction, and (c) transverse z direction in a Mt. Simon sandstone. Velocity of particle is normalized by average velocity of the nanoparticle in that direction. Normalized velocity autocorrelation function along (d) longitudinal direction (VACF$_L$), (e) transverse direction (VACF$_T$). (f) Normalized longitudinal and transverse dispersion coefficient vs Pe in non-Newtonian (NN) fluids and a Mt. Simon sandstone estimated using MSD method and VACF method.
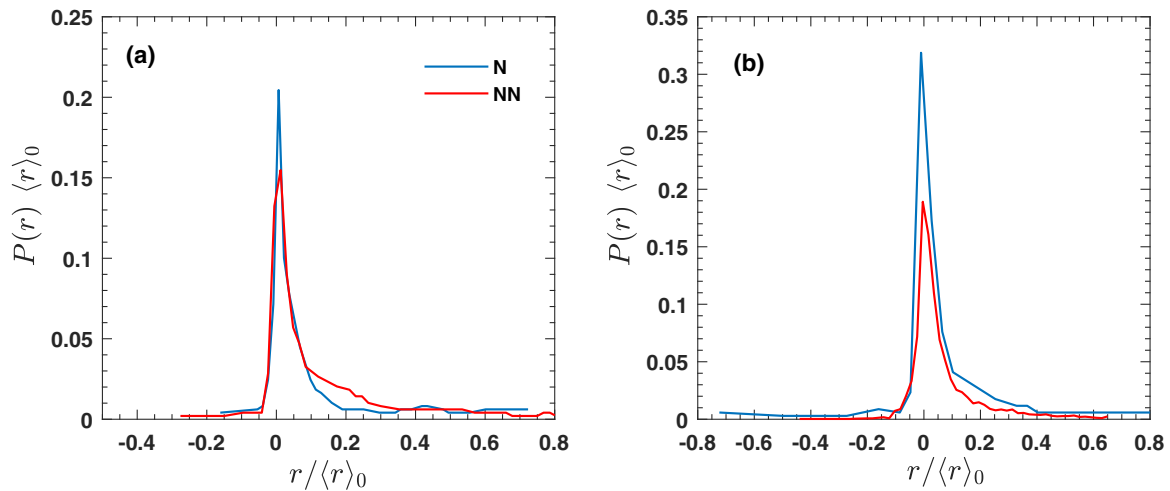

FIG. 8. Probability of particles displacement $P(r)$ as a function of displacement r in (a) a 2D homogeneous porous medium and (b) a Mt. Simon sandstone at $t_D = 6$ and $Pe = 6.28 \times 10^6$ in Newtonian (N) and non-Newtonian (NN) fluids. The coordinates are rescaled by mean displacement $\langle r \rangle_0$.
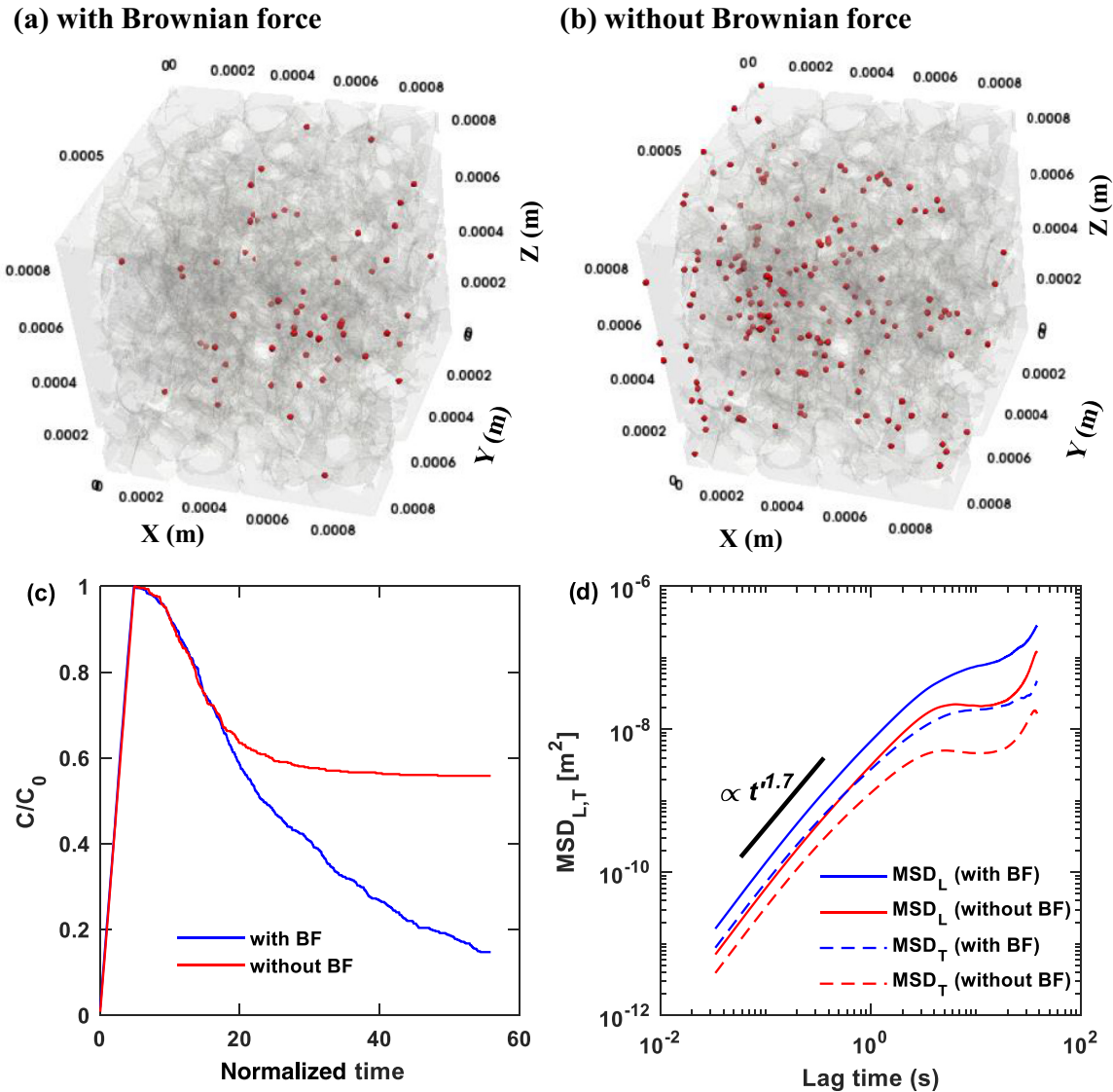
FIG. 9. Spatial distribution of nanoparticles in Mt. Simon sandstone at normalized time of 60, (a) with and (b) without Brownian force. (c) Normalized resident concentration of nanoparticles as a function of dimensionless time (t_D). (d) Mean-square displacement (MSD) along longitudinal direction and transverse direction with and without Brownian force in non-Newtonian fluid (Pe $= 1.26 \times 10^6$). Black line indicate that short time MSD is function of $t'^{1.7}$, suggesting superdiffusive dispersion along longitudinal and transverse direction.

fluids [see Figs. 4(g) and 4(h)]. Our results are in contrast with the result of Refs. [12,24]. Scholz *et al.* [12] observed higher dispersion of nanoparticles for elastic non-Newtonian fluids and homogeneous porous media due to elastic turbulence. Babayekhorasani *et al.* [24] reported that dispersion of nanoparticle is independent of rheology in disordered porous media at same Pe.

Figures 7(a)–7(c) show the distribution of the velocities of nanoparticles in longitudinal and transverse directions normalized by the average velocity of all nanoparticles in the domains considered. The distribution of velocity along the longitudinal direction is skewed non-Gaussian with an exponential stretch in the positive direction. Although velocity distributions of nanoparticles along transverse y and z directions do not overlap, both are symmetric about zero velocity and are non-Gaussian. Nanoparticles along longitu-

dinal direction are channelized along flow direction and thus, it has skewed profile along the positive direction. Whereas, in transverse directions, distributions are non-Gaussian and symmetric. These results are similar to the observation of Refs. [2,3,24].

Figures 7(d) and 7(e) show the normalized autocorrelation function (VACF) over a range of Pe in the non-Newtonian fluid. We normalized lag time using $\frac{t V_{avg}}{\delta_L}$. The longitudinal velocity autocorrelation function indicates a positive correlation over the range of Pe's, whereas the transverse velocity autocorrelation function indicates no significant correlation. Since fluid injection velocity is relatively high, advection plays the dominant role in nanoparticle migration, and most nanoparticles move along the fluid flow directions. This leads to a positive correlation along longitudinal directions.
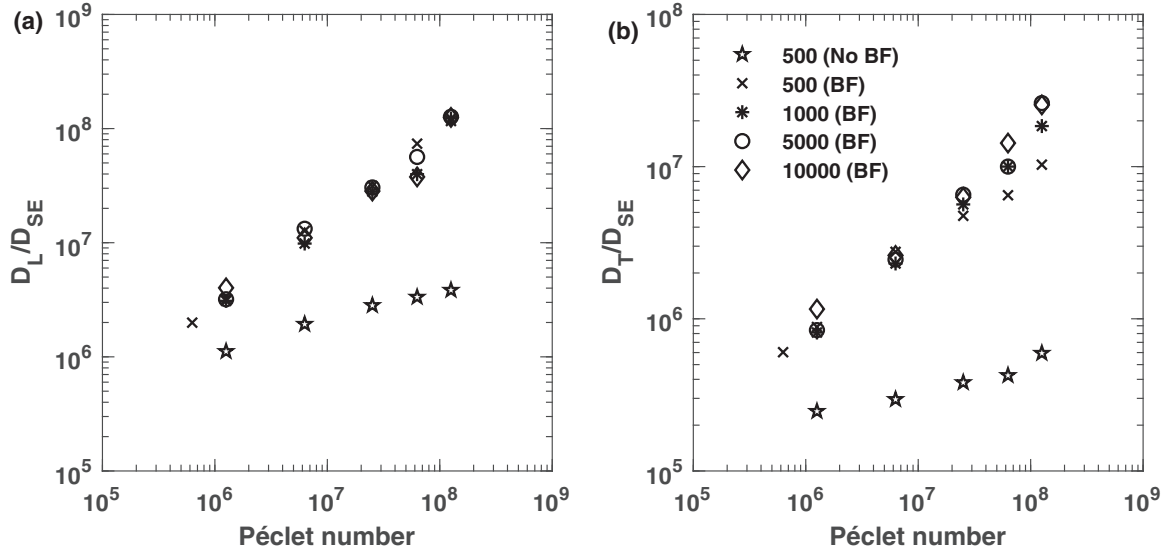
FIG. 10. Effect of nanoparticles concentration and Brownian force (BF) on normalized dispersion coefficient along (a) longitudinal direction and (b) transverse direction in non-Newtonian (NN) fluid and Mt. Simon Simon sandstone. Each symbol represent number of nanoparticles injected per second.

We determined dispersion coefficient along the longitudinal and the transverse directions by fitting a linear-part of MSD curve to $2D_{L,T} t'$. We compared dispersion computed using MSD with long-time dispersion coefficient estimated using a velocity autocorrelation function (VACF). We obtained a similar dispersion coefficient using both methods with a difference of less than 10%. Figure 7(f) depicts dispersion coefficients versus Pe estimated using the VACF method and MSD method for the non-Newtonian fluid.

C. Particle displacement distribution

The mean averaged displacement of particles in a heterogeneous porous medium as measured by Ref. [40] using pulsed-field gradient nuclear magnetic resonance has been used by Refs. [80,81] to validate lattice Boltzmann solute transport simulations and by Ref. [41] to validate OpenFOAM simulations. We note that we have injected 10 000 nanoparticles at the inlet of a 2D homogeneous porous medium and Mt. Simon sandstone, whereas the solute was uniformly distributed in the porous media domain at the start of experiments by Refs. [40,41,80]. Thus, our results could not quantitatively match those of Refs. [40,41,80].

The displacement probability (propagator) for Newtonian and non-Newtonian fluids is plotted at the same flow condition, i.e., at Pe = 6.28×10^6. Figure 8 shows that the distribution of Newtonian and non-Newtonian fluids is non-Gaussian, indicating non-Fickian behavior in both 2D homogeneous porous medium and 3D Mt. Simon sandstone. This result suggests that pore-scale confinement is the dominant factor compared to fluid characteristics, leading to non-Fickian behavior. These results partially agree with the results of Refs. [40,41,80], which suggest heterogeneity-dependent non-Fickian transport of solute in porous media. Similar to the observation of Refs. [40,41] for heterogeneous sandstone and carbonate rock, we observed a large number of

immobile regions with very slow velocity in the Mt. Simon sandstone pore, as described in Fig. 5. Figure 3(c) depicts immobile (very slow velocity) regions before and after the circular solid boundary of a 2D homogeneous porous medium along fluid flow directions. The large peak in Fig. 8 could be attributed to these immobile regions. This result implies that a large immobile region in a confined porous medium gives anomalous behavior for nanoparticle transport in both Newtonian and non-Newtonian fluids. Furthermore, Fig. 8 shows that the stagnation of the propagator distribution is more significant for Newtonian fluids as compared to non-Newtonian fluids in both homogeneous and heterogeneous porous media. This could be due to the higher viscosity of Newtonian fluid in pore space during fluid flow as compared to the inelastic non-Newtonian fluids.

D. Effect of Brownian motion and nanoparticle concentrations

We injected 500 nanoparticles for 1 s in Mt. Simon sandstone over a range of Pe's with and without Brownian force. Figures 9(a) and 9(b) show spatial distribution of nanoparticles at normalized time of 60 and Pe of 1.26×10^6. The normalized resident concentration of nanoparticles [Fig. 9(c)] in sandstone indicates that more than 58% of the nanoparticles are still trapped in the sandstone due absence of Brownian force. These results imply that the nanoparticles' Brownian motion helps nanoparticles migrate from the confined region to the fluid flow region. Furthermore, the Brownian motion of nanoparticles in the heterogeneous porous medium influences pore-accessibility. The mean-square displacement of nanoparticles with Brownian force is much larger than nanoparticles without Brownian force [see Fig. 9(d)]. Figure 10 shows that dispersion of nanoparticles (D_L, D_T) with Brownian force in the heterogeneous porous medium is 1–2 orders of magnitude larger than the dispersion of nanoparticles without Brownian force over a range of Pe's.

To evaluate the effect of nanoparticles concentration on dispersion, we injected 1000, 5000, and 10 000 nanoparticles per second along with non-Newtonian fluid in Mt. Simon sandstone over a range of Pe's. Figure 10(a) shows insignificant variation of D_L over a range of Pe's and nanoparticle concentrations. However, Fig. 10(b) indicates significant increase in D_T with increase in nanoparticle concentration at Pe higher than 10^7.

Contrary to the earlier experimental observations of Refs. [2,3,24], we did not observe the collapse of normalized dispersion coefficients on a single master curve over a range of Pe and porous medium geometries. These results imply that the gradient of shear stress affects the dispersion coefficient in three-dimensional space. Furthermore, although earlier experimental works [2,3,24] were carried out in 3D, the measurement of nanoparticle displacement was carried out in 2D. Thus, the measurement of nanoparticle displacement in transverse z direction was missing.

VI. CONCLUSIONS AND FUTURE WORK

We have shown that the Eulerian-Lagrangian approach can be adopted to study nanoparticles transport and dispersion in an inelastic non-Newtonian fluid (described by Meter model fluid) and heterogeneous porous media in 3D.

Measurements of nanoparticle transport in 3D provide insights into nanoparticles dispersion in the longitudinal and transverse directions. We found that nanoparticles adopt different flow paths in the porous medium at different Péclet numbers due to the porous medium's pore-scale spatial heterogeneity. Lower shear stress of the fluid in the stagnant zone creates resistance for nanoparticles to access pores in stagnant zones in heterogeneous porous media. The Brownian motion of nanoparticles increases the dispersion of nanoparticles along the longitudinal and transverse direction.

Most non-Newtonian fluids are viscoelastic [32]. Previous studies have shown that viscoelastic fluids exhibit elastic turbulence with low Reynolds number flows [3,28,32]. Therefore, in future, we will develop the Eulerian-Lagrangian method to simulate the transport of nanoparticles in a non-Newtonian viscoelastic fluid modeled using the Phan-Thien-Tanner fluid model. This will help to understand the effect of pore-scale viscoelasticity on the dispersion of nanoparticles in 3D heterogeneous porous media.

[1] F. Del Giudice, G. Romeo, G. D'Avino, F. Greco, P. A. Netti, and P. L. Maffettone, Particle alignment in a viscoelastic liquid flowing in a square-shaped microchannel, Lab Chip **13**, 4263 (2013).

[2] F. Babayekhorasani, D. E. Dunstan, R. Krishnamoorti, and J. C. Conrad, Nanoparticle diffusion in crowded and confined media, Soft Matter **12**, 8407 (2016).

[3] J. D. C. Jacob, R. Krishnamoorti, and J. C. Conrad, Particle dispersion in porous media: Differentiating effects of geometry and fluid rheology, Phys. Rev. E **96**, 022610 (2017).

[4] R. Poling-Skutvik, K. I. S. Mongcopa, A. Faraone, S. Narayanan, J. C. Conrad, and R. Krishnamoorti, Structure and dynamics of interacting nanoparticles in semidilute polymer solutions, Macromolecules **49**, 6568 (2016).

[5] J. Zhou and I. Papautsky, Viscoelastic microfluidics: Progress and challanges, Microsyst. Nanoeng. **6**, 113 (2020).

[6] D. Herman and J. Y. Walz, Adsorption and stabilizing effects of highly charged latex nanoparticles in dispersions of weakly-charged silica colloids, J. Colloid Interface Sci. **449**, 143 (2015).

[7] A. Agi, R. Junin, and A. Gbadamosi, Mechanism governing nanoparticle flow behaviour in porous media: Insight for enhanced oil recovery applications, Int. Nano Lett. **8**, 49 (2018).

[8] E. Nourafkan, Z. Hu, and D. Wen, Nanoparticle-enabled delivery of surfactants in porous media, J. Colloid Interface Sci. **519**, 44 (2018).

[9] N. C. Mueller and B. Nowack, Nanoparticles for remediation: Solving big problems with little particles, Elements **6**, 395 (2010).

[10] W. Tungittiplakorn, L. W. Lion, C. Cohen, and J.-Y. Kim, Engineered polymeric nanoparticles for soil remediation, Environ. Sci. Technol. **38**, 1605 (2004).

[11] H. Wu and D. K. Schwartz, Nanoparticle tracking to probe transport in porous media, Acc. Chem. Res. **53**, 2130 (2020).

[12] C. Scholz, F. Wirner, J. R. Gomez-Solano, and C. Bechinger, Enhanced dispersion by elastic turbulence in porous media, Europhys. Lett. **107**, 54003 (2014).

[13] F. Del Giudice, G. D'Avino, F. Greco, P. L. Maffettone, and A. Q. Shen, Fluid Viscoelasticity Drives Self-Assembly of Particle Trains in a Straight Microfluidic Channel, Phys. Rev. Appl. **10**, 064058 (2018).

[14] P. Saffman, A theory of dispersion in a porous medium, J. Fluid Mech. **6**, 321 (1959).

[15] M. J. Skaug, L. Wang, Y. Ding, and D. K. Schwartz, Hindered nanoparticle diffusion and void accessibility in a three-dimensional porous medium, ACS Nano **9**, 2148 (2015).

[16] R. Raccis, A. Nikoubashman, M. Retsch, U. Jonas, K. Koynov, H.-J. Butt, C. N. Likos, and G. Fytas, Confined diffusion in periodic porous nanostructures, ACS Nano **5**, 4607 (2011).

[17] I. C. Kim and S. Torquato, Diffusion of finite-sized Brownian particles in porous media, J. Chem. Phys. **96**, 1498 (1992).

[18] H. Shen, L. J. Tauzin, R. Baiyasi, W. Wang, N. Moringo, B. Shuang, and C. F. Landes, Single particle tracking: From theory to biophysical applications, Chem. Rev. **117**, 7331 (2017).

[19] R. Metzler, J.-H. Jeon, A. G. Cherstvy, and E. Barkai, Anomalous diffusion models and their properties: Nonstationarity, non-ergodicity, and ageing at the centenary of single particle tracking, Phys. Chem. Chem. Phys. **16**, 24128 (2014).

[20] D. Wang, H. Wu, L. Liu, J. Chen, and D. K. Schwartz, Diffusive Escape of a Nanoparticle from a Porous Cavity, Phys. Rev. Lett. **123**, 118002 (2019).

[21] M. Babaei and V. Joekar-Niasar, A transport phase diagram for pore-level correlated porous media, Adv. Water Resour. **92**, 23 (2016).

[22] N. K. Karadimitriou, V. Joekar-Niasar, M. Babaei, and C. A. Shore, Critical role of the immobile zone in non-Fickian two-phase transport: A new paradigm, Environ. Sci. Technol. **50**, 4384 (2016).

[23] S. Hasan, V. Niasar, N. K. Karadimitriou, J. R. Godinho, N. T. Vo, S. An, A. Rabbani, and H. Steeb, Direct characterization of solute transport in unsaturated porous media using fast x-ray synchrotron microtomography, Proc. Natl. Acad. Sci. USA **117**, 23443 (2020).

[24] F. Babayekhorasani, D. E. Dunstan, R. Krishnamoorti, and J. C. Conrad, Nanoparticle dispersion in disordered porous media with and without polymer additives, Soft Matter **12**, 5676 (2016).

[25] R. Maitri, S. De, S. Koesen, H. Wyss, J. Van Der Schaaf, J. Kuipers, J. Padding, and E. Peters, Effect of microchannel structure and fluid properties on non-inertial particle migration, Soft Matter **15**, 2648 (2019).

[26] S. Aramideh, P. P. Vlachos, and A. M. Ardekani, Nanoparticle dispersion in porous media in viscoelastic polymer solutions, J. Non-Newton. Fluid Mech. **268**, 75 (2019).

[27] D. M. Walkama, N. Waisbord, and J. S. Guasto, Disorder Suppresses Chaos in Viscoelastic Flows, Phys. Rev. Lett. **124**, 164501 (2020).

[28] C. A. Browne, A. Shih, and S. S. Datta, Bistability in the unstable flow of polymer solutions through pore constriction arrays, J. Fluid Mech. **890**, A2 (2020).

[29] C. C. Hopkins, S. J. Haward, and A. Q. Shen, Tristability in Viscoelastic Flow Past Side-by-Side Microcylinders, Phys. Rev. Lett. **126**, 054501 (2021).

[30] D. W. Carlson, A. Q. Shen, and S. J. Haward, Microtomographic particle image velocimetry measurements of viscoelastic instabilities in a three-dimensional microcontraction, J. Fluid Mech. **923**, R6 (2021).

[31] S. J. Haward, C. C. Hopkins, and A. Q. Shen, Stagnation points control chaotic fluctuations in viscoelastic porous media flow, Proc. Natl. Acad. Sci. USA **118**, e2111651118 (2021).

[32] C. A. Browne, A. Shih, and S. S. Datta, Pore-scale flow characterization of polymer solutions in microfluidic porous media, Small **16**, 1903944 (2020).

[33] J. M. Ramirez, E. A. Thomann, E. C. Waymire, J. Chastanet, and B. D. Wood, A note on the theoretical foundations of particle tracking methods in heterogeneous porous media, Water Resour. Res. **44**, W01501 (2008).

[34] M. Moroni, N. Kleinfelter, and J. H. Cushman, Analysis of dispersion in porous media via matched-index particle tracking velocimetry experiments, Adv. Water Resour. **30**, 1 (2007).

[35] N. H. Pham and D. V. Papavassiliou, Nanoparticle transport in heterogeneous porous media with particle tracking numerical methods, Comput. Particle Mech. **4**, 87 (2017).

[36] D. Mangal, J. C. Conrad, and J. C. Palmer, Nanoparticle dispersion in porous media: Effects of hydrodynamic interactions and dimensionality, AIChE J. **67**, e17147 (2021).

[37] D. Mangal, J. C. Palmer, and J. C. Conrad, Nanoparticle dispersion in porous media: Effects of array geometry and flow orientation, Phys. Rev. E **104**, 015102 (2021).

[38] G. Li, G. H. McKinley, and A. M. Ardekani, Dynamics of particle migration in channel flow of viscoelastic fluids, J. Fluid Mech. **785**, 486 (2015).

[39] M. Moroni, J. Cushman, and A. Cenedese, A 3D-PTV two-projection study of pre-asymptotic dispersion in porous media

which are heterogeneous on the bench scale, Int. J. Eng. Sci. **41**, 337 (2003).

[40] U. Scheven, D. Verganelakis, R. Harris, M. Johns, and L. Gladden, Quantitative nuclear magnetic resonance measurements of preasymptotic dispersion in flow through porous media, Phys. Fluids **17**, 117107 (2005).

[41] B. Bijeljic, A. Raeini, P. Mostaghimi, and M. J. Blunt, Predictions of non-Fickian solute transport in different classes of porous media using direct simulation on pore-scale images, Phys. Rev. E **87**, 013011 (2013).

[42] D. M. Meter and R. B. Bird, Tube flow of non-Newtonian polymer solutions: Part I. Laminar flow and rheological models, AIChE J. **10**, 878 (1964).

[43] T. Shende, V. J. Niasar, and M. Babaei, Effective viscosity and Reynolds number of non-Newtonian fluids using meter model, Rheol. Acta **60**, 11 (2021).

[44] T. Shende, V. Niasar, and M. Babaei, Upscaling non-Newtonian rheological fluid properties from pore-scale to Darcy's scale, Chem. Eng. Sci. **239**, 116638 (2021).

[45] F. Greifzu, C. Kratzsch, T. Forgber, F. Lindner, and R. Schwarze, Assessment of particle-tracking models for dispersed particle-laden flows implemented in OpenFOAM and ANSYS FLUENT, Eng. Appl. Comput. Fluid Mech. **10**, 30 (2016).

[46] C. Fernandes, D. Semyonov, L. L. Ferrás, and J. M. Nóbrega, Validation of the CFD-DPM solver DPMFoam in OpenFOAM through analytical, numerical and experimental comparisons, Granular Matter **20**, 64 (2018).

[47] K. Jang, W. Han, and K. Y. Huh, Simulation of a moving-bed reactor and a fluidized-bed reactor by DPM and MPPIC in OpenFOAM, in *OpenFOAM* (Springer, Berlin, 2019), pp. 419–435

[48] C. T. Crowe, J. D. Schwarzkopf, M. Sommerfeld, and Y. Tsuji, *Multiphase Flows with Droplets and Particles* (CRC Press, Boca Raton, FL, 2011).

[49] A. Li and G. Ahmadi, Dispersion and deposition of spherical particles from point sources in a turbulent channel flow, Aerosol Sci. Technol. **16**, 209 (1992).

[50] P. Pálovics and M. Rencz, Investigation of the motion of magnetic nanoparticles in microfluidics with a micro domain model, Microsyst. Technol. **28**, 1545 (2022).

[51] X. Meng, Coupling of nanofluid flow, heat transfer, and nanoparticles sedimentation using OpenFOAM, Ph.D. thesis, City, University of London, 2017.

[52] P. A. Cundall and O. D. Strack, A discrete numerical model for granular assemblies, Geotechnique **29**, 47 (1979).

[53] F. Moukalled, L. Mangani, M. Darwish *et al.*, *The Finite Volume Method in Computational Fluid Dynamics*, Vol. 113 (Springer, Berlin, 2016).

[54] J. H. Ferziger, M. Perić, and R. L. Street, *Computational Methods for Fluid Dynamics*, Vol. 3 (Springer, Berlin, 2002).

[55] A. H. Kohanpur, M. Rahromostaqim, A. J. Valocchi, and M. Sahimi, Two-phase flow of CO_2-brine in a heterogeneous sandstone: Characterization of the rock and comparison of the lattice-Boltzmann, pore-network, and direct numerical simulation methods, Adv. Water Resour. **135**, 103469 (2020).

[56] D. Kawale, E. Marques, P. L. Zitha, M. T. Kreutzer, W. R. Rossen, and P. E. Boukany, Elastic instabilities during the flow of hydrolyzed polyacrylamide solution in porous media: effect of pore-shape and salt, Soft Matter **13**, 765 (2017).

[57] S. De, J. Kuipers, E. Peters, and J. Padding, Viscoelastic flow simulations in random porous media, J. Non-Newton. Fluid Mech. **248**, 50 (2017).

[58] J. Savins, Non-Newtonian flow through porous media, Ind. Eng. Chem. **61**, 18 (1969).

[59] K. S. Sorbie, *Polymer-improved Oil Recovery* (Springer Science & Business Media, Berlin, 2013).

[60] C. Xie, W. Lv, and M. Wang, Shear-thinning or shear-thickening fluid for better EOR?—A direct pore-scale study, J. Pet. Sci. Eng. **161**, 683 (2018).

[61] A. H. Slim, R. Poling-Skutvik, and J. C. Conrad, Local confinement controls diffusive nanoparticle dynamics in semidilute polyelectrolyte solutions, Langmuir **36**, 9153 (2020).

[62] R. S. Maier, D. M. Kroll, R. S. Bernard, S. E. Howington, J. F. Peters, and H. T. Davis, Pore-scale simulation of dispersion, Phys. Fluids **12**, 2065 (2000).

[63] J. G. Oldroyd, On the formulation of rheological equations of state, Proc. R. Soc. London A **200**, 523 (1950).

[64] H. Giesekus, A simple constitutive equation for polymer fluids based on the concept of deformation-dependent tensorial mobility, J. Non-Newton. Fluid Mech. **11**, 69 (1982).

[65] N. P. Thien and R. I. Tanner, A new constitutive equation derived from network theory, J. Non-Newton. Fluid Mech. **2**, 353 (1977).

[66] E. Boek, J. Padding, V. Anderson, P. Tardy, J. Crawshaw, and J. Pearson, Constitutive equations for extensional flow of worm-like micelles: Stability analysis of the Bautista–Manero model, J. Non-Newton. Fluid Mech. **126**, 39 (2005).

[67] R. B. Bird, R. C. Armstrong, and O. Hassager, *Dynamics of Polymeric Liquids. Vol. 1: Fluid Mechanics* (John Wiley and Sons, New York, NY, 1987).

[68] T. Shende, V. Niasar, and M. Babaei, Pore-scale simulation of viscous instability for non-Newtonian two-phase flow in porous media, J. Non-Newton. Fluid Mech. **296**, 104628 (2021).

[69] S. An, M. Sahimi, T. Shende, M. Babaei, and V. Niasar, Enhanced thermal fingering in a shear-thinning fluid flow through porous media: Dynamic pore network modeling, Phys. Fluids **34**, 023105 (2022).

[70] F. Pimenta and M. Alves, Stabilization of an open-source finite-volume solver for viscoelastic fluid flows, J. Non-Newton. Fluid Mech. **239**, 85 (2017).

[71] M. Alves, P. Oliveira, and F. Pinho, Numerical methods for viscoelastic fluid flows, Annu. Rev. Fluid Mech. **53**, 509 (2021).

[72] F. Pimenta and M. Alves, rheotool, https://github.com/fppimenta/rheoTool (2016).

[73] See Supplemental Material at http://link.aps.org/supplemental/10.1103/PhysRevE.106.015103 for movies.

[74] M. Villone, G. D'Avino, M. Hulsen, F. Greco, and P. Maffettone, Simulations of viscoelasticity-induced focusing of particles in pressure-driven microslit flow, J. Non-Newton. Fluid Mech. **166**, 1396 (2011).

[75] G. Romeo, G. D'Avino, F. Greco, P. A. Netti, and P. L. Maffettone, Viscoelastic flow-focusing in microchannels: Scaling properties of the particle radial distributions, Lab Chip **13**, 2802 (2013).

[76] D. Yuan, Q. Zhao, S. Yan, S.-Y. Tang, G. Alici, J. Zhang, and W. Li, Recent progress of particle migration in viscoelastic fluids, Lab Chip **18**, 551 (2018).

[77] G. D'Avino, G. Romeo, M. M. Villone, F. Greco, P. A. Netti, and P. L. Maffettone, Single line particle focusing induced by viscoelasticity of the suspending liquid: Theory, experiments, and simulations to design a micropipe flow-focuser, Lab Chip **12**, 1638 (2012).

[78] Y.-F. Chen, H.-H. Wei, Y.-J. Sheng, and H.-K. Tsao, Superdiffusion in dispersions of active colloids driven by an external field and their sedimentation equilibrium, Phys. Rev. E **93**, 042611 (2016).

[79] M. A. Zaks and A. Nepomnyashchy, Subdiffusive and superdiffusive transport in plane steady viscous flows, Proc. Natl. Acad. Sci. USA **116**, 18245 (2019).

[80] J. Yang, J. Crawshaw, and E. S. Boek, Quantitative determination of molecular propagator distributions for solute transport in homogeneous and heterogeneous porous media using lattice Boltzmann simulations, Water Resour. Res. **49**, 8531 (2013).

[81] E. S. Boek, I. Zacharoudiou, F. Gray, S. M. Shah, J. P. Crawshaw, and J. Yang, Multiphase-flow and reactive-transport validation studies at the pore scale by use of lattice Boltzmann computer simulations, SPE J. **22**, 940 (2017).